Journal of Catalysis 431 (2024) 115389

Contents lists available at ScienceDirect

Journal of Catalysis

journal homepage: www.elsevier.com/locate/jcat

Research article

Surface ZnO_x on zirconia is highly active for high temperature methanol synthesis

M.T. Nikolajsen [a], J.-C. Grivel [b], A. Gaur [c], L.P. Hansen [d], L. Baumgarten [c,e], N.C. Schjødt [d], U. V. Mentzel [d], J.-D. Grunwaldt [c,e], J. Sehested [d], J.M. Christensen [a], M. Høj [a,*]

[a] Department of Chemical and Biochemical Engineering, Technical University of Denmark (DTU), Kgs. Lyngby 2800, Denmark
[b] Department of Energy Conversion and Storage, Technical University of Denmark (DTU), Kgs. Lyngby 2800, Denmark
[c] Institute for Chemical Technology and Polymer Chemistry (ITCP), Karlsruhe Institute of Technology (KIT), Karlsruhe 76131, Germany
[d] Topsoe A/S, Kgs. Lyngby 2800, Denmark
[e] Institute of Catalysis Research and Technology (IKFT), Karlsruhe Institute of Technology (KIT), Karlsruhe 76131, Germany

ARTICLE INFO

Keywords:
Carbon dioxide
Methanol
Zinc
Zirconia

ABSTRACT

Zinc containing mixed metal oxides and supported zinc oxide are stable and selective methanol synthesis catalysts at temperatures where a subsequent methanol to hydrocarbons reaction can occur directly. This work provides fundamental insights into ZnO-based high temperature methanol synthesis catalysts. A pronounced support effect was observed, where ZrO_2 provided a beneficial effect while SiO_2 exerted a detrimental effect compared to bulk ZnO. Preparing co-precipitated ZnO-ZrO_2 catalysts showed that the initial activity correlated with the amount of amorphous ZnO on the surface of the support and that the catalytic activity increased with time on stream as zinc oxide migrated out of a solid solution with ZrO_2 and onto the support surface. Hence the active phase appeared to be ZnO surface species and not zinc oxide in a solid solution with ZrO_2. Operando XAS coupled with modulation excitation spectroscopy unravelled that the surface ZnO was partly reduced under operating conditions, as surface ZnO_x, with x approximately equal to 0.98. In-situ DRIFTS further uncovered that the surface ZnO_x activated CO_2 and formed methanol via carbonate, formate and methoxide species. XPS finally showed that ZrO_2 withdrew electrons from ZnO, facilitating oxygen abstraction to form the partly reduced ZnO_x, which in turn facilitated the activation of CO_2.

1. Introduction

Polymeric materials play an important role in society's permanently evolving needs and challenges because they are versatile, durable, and adaptable. From 1950 to 2019, the global production of polymeric materials increased from 2 Mt to 460 Mt, and the worldwide consumption is forecasted to be 590 Mt in 2030 [1,2]. In 2019 polyethylene, polypropylene, polystyrene, and polyethylene terephthalate accounted for 229 Mt [3]. These products are directly related to the monomers ethylene, propylene, ethenyl benzene, and *para*-xylene. Since these chemicals are mainly produced from crude oil, the demand for an alternative feedstock is increasing as a part of an effort to reduce global CO_2 emissions[4].

CO_2 generated from biomass or captured from the atmosphere or at a point source can be utilized to produce these monomers or monomer precursors mentioned above. A route for utilizing CO_2 is the combination of methanol synthesis and methanol dehydration to hydrocarbons. The methanol synthesis is equilibrium limited, but a strategy to overcome this, is to combine a methanol synthesis catalyst with a zeolite methanol dehydration catalyst within one reactor [5,6]. The purpose of the zeolite is to ensure immediate conversion of the formed methanol and thereby shift the equilibrium towards the products. At the temperatures necessary for the zeolite to be active (300 to 420 °C), the traditional Cu/ZnO/Al_2O_3 methanol synthesis catalyst cannot be used because severe sintering of the metallic copper deactivates the catalyst [7]. Furthermore, the metallic copper causes hydrogenation of the olefins formed in the zeolite and thus disrupts the formation of unsaturated hydrocarbons [8]. For these reasons, there is currently a significant interest in finding metal oxides with high stability, high methanol synthesis activity and limited olefin hydrogenation activity.

A range of metal oxide catalysts, primarily based on ZnO, have shown high methanol synthesis activity at temperatures above 300 °C

* Corresponding author.
E-mail address: mh@kt.dtu.dk (M. Høj).

https://doi.org/10.1016/j.jcat.2024.115389
Received 11 September 2023; Received in revised form 7 February 2024; Accepted 21 February 2024
Available online 23 February 2024

[5,6,9–12]. Particularly catalysts combining ZnO and ZrO_2 have shown an improved performance. The solid solution of ZnO-ZrO_2 synthesized by Wang et al. [9] demonstrated high methanol selectivity of 86–91 %, achieved with a CO_2 single-pass conversion of more than 10 % (at 50 bar, H_2/CO_2 of 3 to 4, and at 315 to 320 °C). The ZnO-ZrO_2 solid solution kept its activity for 500 h on stream and was resistant to sintering at higher temperatures. Wang et al. [9] suggested that the high methanol selectivity is attributed to the synergetic effect of H_2 activation on zinc sites and simultaneous activation of CO_2 on the neighbouring zirconia site within a solid solution of the two components.

There has been clear evidence that the ZnO-ZrO_2 combination may form a solid solution. Co-precipitating zinc oxide and zirconia produces a material where zinc is stabilizing the tetragonal phase of zirconia. Zirconia exhibits a monoclinic crystal structure at temperatures below 1170 °C, but the introduction of dopants is known to stabilize the metastable tetragonal structure [13]. Several studies have observed a systematic shift in the (1 0 1) Bragg reflection to higher 2θ° with increasing zinc loading until zirconia-zinc saturation ~ 33 mol% Zn [9]. Beyond this saturation, hexagonal zinc oxide starts to form and become visible in XRD [9,14–16]. The systematic shift in the (1 0 1) Bragg reflection is caused by the substitution of Zr^{4+} (84 Å) with Zn^{2+} (74 Å), which shrinks the tetragonal lattice. Similar trends have been observed with the dopants iron- and yttrium oxide with an ionic radius of 70 Å and 90 Å, shifting the (1 0 1) Bragg reflection to higher and lower 2θ°, respectively [17,18]. On ZnO-ZrO_2 catalysts, FTIR bands around 500 and 600–700 cm^{-1} were associated with Zn-O-Zn and Zn-O-Zr vibrations [19] and UV–vis spectra of ZrO_2 changed with Zn as dopant indicated the presence of isolated Zn^{2+} ions [20]. These findings have led to the belief that it is surface available Zn^{2+} embedded in the zirconia crystal lattice, as part of a solid solution, which in synergy with Zr^{4+} is the active site for CO_2 hydrogenation.

By contrast, low Zn-Zn or Zn-Zr coordination numbers found by X-ray absorption spectroscopy [21] and enrichment of Zn on the zirconia surface detected by X-ray photoelectron spectroscopy [9,15] suggest that ZnO is mostly present at the zirconia surface. Even at low Zn content (Zn/Zr = 1/100), individual lattice fringes of isolated ZnO were detected by high-resolution transmission electron microscopy, indicating difficulties for Zn^{2+} to be present inside the ZrO_2 lattice and a preference for generation of a separate ZnO phase [22]. The ZnO-ZrO_2 mixed oxides thus have surface ZnO, which exists apart from the solid solution. Currently there is no clear knowledge about whether the surface ZnO or the Zn^{2+} within a solid solution is the primary active species.

This study aims to bridge this gap by identifying the active species in ZnO-based methanol synthesis catalysts with particular emphasis on ZnO-ZrO_2 mixed oxides prepared by co-precipitation and impregnation. The purpose is to identify good candidates for the bifunctional catalytic system and clarifying the metal oxide structure–activity relation, particularly the relative importance of Zn-Zr solid solution and ZnO surface domains. ZnO was deposited on silica (SiO_2), anatase titania (TiO_2), monoclinic zirconia (m-ZrO_2), and tetragonal zirconia (t-ZrO_2) by the incipient wetness impregnation method and ZnO-ZrO_2 was prepared by co-precipitation. The catalysts were characterized by X-ray diffraction (XRD), inductively coupled plasma optical emission spectroscopy (ICP-OES), X-ray absorption spectroscopy (XAS), X-ray photoelectron spectroscopy (XPS), high-resolution scanning transmission electron microscopy (HR-STEM) and N_2 adsorption/desorption (BET). Furthermore, the reaction species involved in the CO_2 hydrogenation reaction on the surface of the catalyst were analysed by in-situ diffuse reflectance infrared Fourier transform spectroscopy (DRIFTS). The changes in the oxidation state of the supported ZnO was investigated by time resolved QEXAFS coupled with modulation excitation spectroscopy (MES).

2. Materials and method

2.1. Catalyst preparation

A series of ZnO-containing catalysts were prepared by the incipient wetness impregnation method. Firstly, the supports were dried overnight at 120 °C and the precise water uptake was determined of the dried supports. The supports were then impregnated with a solution of Zn $(NO_3)_2{\cdot}6H_2O$ to produce catalysts with 13 mol% Zn (Zn/(M + Zn), where M is Si, Ti or Zr). Finally, the catalysts were dried overnight at 100 °C and calcined in air at 500 °C for five hours. The supports used were SiO_2 255 m^2/g, TiO_2 161 m^2/g, m-ZrO_2 57.2 m^2/g, t-ZrO_2 145 m^2/g (stabilized by Al_2O_3) and t-ZrO_2-CeO_2 105 m^2/g, all provided by Saint-Gobain NorPro. Furthermore, the ZnO content on t-ZrO_2 was varied from 13 to 44 mol%, all produced with the above-mentioned procedure. All impregnated samples are denoted with a forward slash as ZnO/support. All ZrO_2 supported catalysts showed HfO_2 impurity, typically 1–2 mol% Hf.

For comparison, a ZnO-ZrO_2 catalyst was prepared by the co-precipitation method proposed by Wang et al. [9], the hyphen is used here to denote co-precipitation. A 500 mL solution of 5.52 g Zn $(NO_3)_2{\cdot}6H_2O$ and 37.6 g $ZrO(NO_3)_2{\cdot}xH_2O$ was added to a beaker and heated to 70 °C. A 500 mL solution of 15.3 g $(NH_4)_2CO_3$ was added dropwise to the warm precursor solution under vigorous stirring. The mixture was then aged for 120 min at 70 °C, filtered and washed with demineralized water. The collected solid was dried at 100 °C overnight and calcined in air at 500 °C for five hours. Co-precipitation of a similar catalyst was repeated at a precipitation and ageing temperature of 100 °C under reflux and this sample was denoted ZnO-ZrO_2-100.

Pure ZnO was prepared by precipitating $Zn(NO_3)_2{\cdot}6H_2O$ with a Na_2CO_3 solution at pH = 7 and 70 °C. The precipitated ZnO was aged for 60 min at 70 °C and pH = 7, then filtered and washed with demineralized water. The solid was collected and dried overnight at 80 °C and calcined in air at 350 °C for three hours.

2.2. Catalytic activity evaluation

The methanol synthesis activity tests were conducted in a high-pressure flow reactor setup using a quartz-lined reactor tube with an inner diameter of 4 mm. Typically, 300 mg of the catalyst with a grain size of 150–300 μm was loaded into the reactor tube. Synthesis gas CO_2/H_2/Ar with the composition of 20/60/20 vol% at 50 barg was introduced into the reactor at various temperatures in the range 280–400 °C. The reaction temperature was controlled by a N-type thermocouple placed right above the catalyst bed inside the reactor tube and an electric furnace with three heating zones. It should be noted that no pretreatment was given to the catalysts before the catalytic testing. The internal standard, argon, was used for accounting for the decrease in reaction volume. The carbon balance closed at an average of 99.95 % ± 0.99 % for all the experiments. The effluent gas was analysed by an online GC (ThermoFisher Trace 1300, assembled by Global Analyzer Solutions) equipped with a thermal conductivity detector (TCD) and a flame ionization detector (FID). The GC column connected to the flame ionization detector was Rtx-5 (60 m, 0.32 mmID and 5 μm df), which separated the formed products (methane, methanol, and dimethyl ether). A combination of Hayesep N, XL Sulfur and Molsieve 5A columns were connected to the TCD detector for quantification of CO, CO_2, and Ar. The CO_2 conversion, oxygenate (CH_3OH + CH_3OCH_3) selectivity, and oxygenate formation rate was calculated by Eq. (1) to (4).

$$\dot{F}_{i,out} = \dot{V}_{in} \cdot \frac{y_{Ar,in}}{y_{Ar,out}} \cdot y_{i,out} \cdot V_m^{-1} \quad (1)$$

$$X_{CO_2} = 1 - \frac{\dot{F}_{CO_2,out}}{\dot{F}_{CO_2,in}} \quad (2)$$

$$S_{CH_3OH+CH_3OCH_3} = \frac{\dot{F}_{CH_3OH,out} + 2\cdot\dot{F}_{C_2H_6O,out}}{\dot{F}_{CO_2,in} - \dot{F}_{CO_2,out}}\cdot 100\% \quad (3)$$

$$Rate = \frac{\left(\dot{F}_{CH_3OH,out} + 2\cdot\dot{F}_{CH_3OCH_3,out}\right)\cdot M_{w,CH_3OH}}{m_c} \quad (4)$$

Where $\dot{V}$ is the volumetric flow rate at standard conditions, V_m is the molar volume, m_c is the weight of the catalyst, and M_w is the molar mass. $\dot{F}_i$ and y_i is the molar flow rate and molar fraction of component i. Both methanol and dimethyl ether can be further dehydrogenated in zeolites to form hydrocarbons. Therefore, the production of both is relevant to consider when showing the activity of the catalysts.

2.3. Catalyst characterization

XRD analysis was conducted with a PanAlytical X'Pert Pro instrument in Bragg-Brentano geometry in reflectance mode using a Cu K_α radiation source ($\lambda = 1.541$ Å) at ambient conditions. The scan range was 5–70° with a step size of 0.017°. The Rietveld analysis was performed using the Topas software. To analyse the elemental composition, ICP-OES analysis was conducted on an Agilent 700 Series instrument using argon as plasmogene. The specific surface area was analysed with the 3P instrument Sync440 and the N_2 adsorption isotherm was analysed by the Brunauer-Emmett-Teller method.

The XPS measurements were performed in an ultra-high vacuum with an ESCALAB Xi^+ instrument from ThermoFisher Scientific, employing a monochromatic Al K_α (1486.6 eV) X-ray source. The powdered samples were pressed onto a piece of adhesive copper tape (3 M Electrical Tape). The diameter of the analysis area was approximately 650 µm. A low energy electron flood gun was used for the neutralization of surface charge buildup. The binding energies were calibrated by using Au foil ($4f_{7/2}$ binding energy of 83.95 eV). Etching was conducted in Ar cluster mode with an energy of 2000 eV during steps of 30 s and raster size of 3.25 x 3.25 mm^2. The data were analyzed with the Thermo Avantage software.

X-ray absorption spectroscopy (XAS) measurements at the Zn K absorption edge were done in transmission and fluorescence mode at the SuperXAS beamline10A, Swiss Light Source (SLS) synchrotron. QEXAFS spectra were recorded with a frequency of 1 Hz of the monochromator. Data importing and pre-processing involving energy calibration, rebinning, averaging and exporting was done using the ProQEXAFS software developed at the beamline [23]. Basic XAS data treatment of normalization, background subtraction and Fourier transformation has been conducted using Athena [24]. For the ex-situ measurements, pellets were prepared using cellulose diluted catalyst samples pressed as 13 mm diameter, self-sustaining wafers and the energy scanned in transmission mode. By taking average of 400 spectra, the k^3-weighted Fourier transformed EXAFS function (k range 3 to 12 $Å^{-1}$) was fitted in R – space (1 to 3 Å). The wurtzite ZnO structure model (ICSD 67849) was used for fitting the amplitude reduction factor, $S_0^2 = 0.982$, to the obtained reference spectrum of the ZnO sample. This value of amplitude reduction factor was used in the refining of coordination number (CN), interatomic distances (R), energy shift (ΔE_0), and mean square deviation of interatomic distances (σ^2) for the first and second shell of ZnO on the catalyst samples. These fits were performed using Artemis by a least-square method in the R space between 1 and 3.7 Å [24]. The surface zinc oxide did not show a Zn-Zn interaction (CN = 0), meaning that the fraction of the surface sites can be estimated from the coordination number of the second shell as proposed by Han et al. [21] in Eq. (5).

$$\chi(ZnO_x), [\%] = \left(1 - \frac{CN_{Zn-Zn}}{12}\right)\cdot 100\% \quad (5)$$

The coordination number of Zn-Zn in bulk ZnO is 12 and as XAS is a bulk method, the fitted coordination number is an average. The fitting results and the estimated fraction of surface ZnO_x for the catalyst samples can be found in Table S2. Linear combination fitting was conducted using the (0.13)ZnO/t-ZrO_2 (no ZnO was visible from XRD and no Zn-Zn back scattering in FT-EXAFS was observed) and ZnO as references for surface ZnO_x sites and crystalline ZnO respectively and compared to the results obtained by Eq. (5). The weight percentage of surface ZnO_x sites on the zirconia supports was used for calculating the amount of ZnO_x present on the zirconia surface by Eq. (6), as XPS and XRD results suggest no to hardly any incorporation of Zn into the zirconia lattice.

$$n_{ZnO_x}, [\mu mol/g_{cat}] = \frac{b_{Zn}\cdot I_{Zn}}{Mw_{Zn}}\cdot 10^6 \quad (6)$$

Where n_{ZnO_x}, b_{Zn}, I_{Zn}, and Mw_{Zn} are the concentration of surface ZnO_x pr. gram of catalyst, the bulk concentration of Zn determined by ICP-OES, the weight percentage of surface Zn determined by linear combination fitting and the molar mass of Zn, respectively.

For the in-situ experiments, quartz capillaries (length of 80 mm, o.d. 0.8 mm with 0.01 mm wall thickness) were loaded with 4.4 mg 100–200 µm catalyst particles diluted 1:4 in inert α-Al_2O_3 giving a bed length of 7 mm. To ensure a pressure tolerance of 20 bar, the loaded capillaries were glued using Araldite Rapid Epoxy to a sample holder and cured for several hours. Hereafter, the sample holder was connected to the flow setup, where a downstream mass spectrometer and 10 % CO/He, CO_2, 10 % O_2/He and He gasses were connected. The capillaries were heated by radiative heaters provided by the beamline. The experimental procedure included dehydration of the catalysts in O_2/He with a heating ramp of 10 °C /min to 400 °C at 15 bar, followed by cooling to room temperature. Then the gas was switched to a syngas mixture ($CO/CO_2/H_2$/He = 5/12/37/46, filtered through an active carbon filter to remove nickel carbonyls) and when a stable MS signal was achieved, the reactor was heated to 400 °C at 10 °C /min and kept at 400 °C for 2 h. Thirdly, the modulation excitation spectroscopy (MES) coupled XAS experiments were performed where the gas was switched between O_2/He and syngas in intervals of 10 min at 400 °C and 15 bar. One cycle refers to the total time of O_2/He and syngas exposure (10 min in O_2/He and 10 min in syngas) and the switching was repeated for a total of 9 cycles. For the MES experiment, a four-way valve was used to switch the flow to the capillary between the two gas mixtures, allowing the flow of one gas mixture to the reactor and the other to a purge line. To avoid pressure fluctuations, the pressure of the purge line was adjusted by a back-pressure valve to 15 bar, keeping the reactor and the purge line pressure almost equal. Time resolved spectra were continuously recorded in transmission as well as fluorescence mode in the middle of the catalytic bed through all the above-mentioned steps. For the MES analysis, florescence spectra were used due to high spectral quality. The oscillation frequency of the monochromator was fixed at 1 Hz, leading to a spectrum acquisition every 500 ms. Thus, the 20 min cycle (1 period) produced around 2400 spectra, meaning a total of 21,600 spectra for 9 periods, were generated during each MES experiment. For the MES data analysis, normalized spectra were first averaged in 20 s intervals to obtain 60 time-resolved spectra for each cycle. This averaging enhanced the signal-to-noise ratio for detection of small changes during the switching [25]. The time-resolved spectra were transformed into phase-resolved spectra μ(E, Δϕ) using Eq. (7) [26–28]. This creates a phase-resolved set of spectra at different phase shifts $0° \leq \Delta\phi < 360°$ based on the sine function of cycle time, T = 1200 s. Changes occurring at identical phase shifts during each cycle were added making small changes detectable. The changes observed from the phase-resolved spectra were analyzed qualitatively and quantitatively by comparing them to the spectra of ZnO and (0.13)ZnO/t-ZrO_2 subtracted by Zn foil.

$$\mu(E,\Delta\phi) = \frac{2}{T}\int_0^T \mu(E,t)\cdot\sin\left(\frac{360^\circ}{T}t + \Delta\phi\right)dt \quad (7)$$

Transmission electron microscopy imaging of the catalysts were per-

formed on a Thermo Fisher Spectra 200 X-CFEG (S)TEM microscope equipped with Dual-X EDS detectors. The catalyst samples were crushed in a mortar and dispersed in absolute ethanol (99.9 %) before drop casting on a Cu-TEM grid covered with lacey carbon film (SPI supplies). Images and energy dispersive X-ray (EDX) spectroscopy maps were acquired in scanning transmission mode (STEM) with a probe current of 0.2nA and a probe convergence angle of 30 mrad. Detector collection angles of 0–22 mrad and 56–200 mrad were applied for the bright-field (BF) and high-angular annular dark field (HAADF) detector, respectively. The EDX maps were acquired continuously scanning for >10 min to obtain decent signals and were post-processed in Velox 3.8 to generate element composite images with pixel-averaged smoothing.

The reaction mechanism of CO_2 hydrogenation over (0.13)ZnO/t-ZrO_2 was probed by CO_2 adsorption, steady-state methanol synthesis, He and H_2 temperature-programmed-desorption/reaction with the use of in-situ diffuse reflectance infrared Fourier transform spectroscopy (DRIFTS). A Harrick high pressure Praying Mantis cell equipped with a high pressure dome and pure ZnSe windows was placed in a Vertex 70 infrared spectrometer with a liquid nitrogen cooled LN-MCT VP detector. The loaded sample was pretreated under He flow at 400 °C and 20 bar for 2 h and then cooled to the reaction temperature, where a background spectrum was acquired. For the CO_2 adsorption experiment, the gas was switched to CO_2/He where the development of peaks was continuously monitored for 60 min. Hereafter, the gas was switched to H_2/He and the change and disappearance of surface species were continuously monitored for 60 min. For the steady-state methanol synthesis experiment, after the pretreatment, the gas was switched to CO_2/H_2/He (13/38/49 vol%) and DRIFTS spectra were recorded for 60 min. After the steady-state methanol synthesis experiment, the reactor was cooled to room temperature and the gas was switched to either pure He or H_2. When a stable MS signal was achieved, the temperature was increased to 420 °C by ~ 6 °C/min.

3. Results and discussion

3.1. Support effects in ZnO catalysed CO_2 hydrogenation

Firstly, the catalytic activity as function of temperature from 280 to 400 °C was measured (Fig. S1). These temperatures are above those applied in industrial methanol synthesis, but relevant temperatures for subsequent methanol dehydration to hydrocarbons over zeolites. The results showed that at temperatures $\geq$ 360 °C the gas composition reached equilibrium, thus these results cannot be used for comparing the activity of the catalysts. The CO_2 hydrogenation activity results reported in the following were obtained at 320 °C, where both the reverse-water–gas-shift (RWGS) and the methanol synthesis were far from equilibrium (see calculations of approach to equilibrium in Table S1). Results with/without pre-reduction of the catalyst with hydrogen showed that the effect of this pre-treatment was negligible (see Fig. S2). Next, the effect of the feed gas composition was investigated, and it was found that the partial pressures of CO_2 and H_2 were crucial for the methanol synthesis activity over ZnO supported on zirconia. Shifting from a feed of CO/H_2 to CO_2/H_2 increased the activity dramatically (Fig. S3 and Fig. S5). Co-feeding or partially replacing CO_2 with CO did not improve the catalytic activity (Fig. S4), suggesting that the primary carbon source for methanol formation is CO_2, as also seen for Cu/ZnO based catalysts [29]. Increasing the H_2/CO_x ratio also increased the rate of methanol synthesis (Fig. S5).

The oxygenate (methanol + dimethyl ether (DME)) formation rate (Eq. (3)) and selectivity (Eq.(4)) over supported zinc oxide catalysts at 320 °C are shown in Fig. 1. The results reveal a clear support effect in the ZnO catalysed methanol synthesis. Supporting zinc oxide on anatase titania or monoclinic- and tetragonal zirconia significantly increased the oxygenate formation rate compared to bulk zinc oxide. This improvement was partly due to an increase in the CO_2 conversion, but mostly due to the enhanced oxygenate selectivity, which increased from 34 % for ZnO to 68–80 % for supported zinc oxide. The DME selectivity was lower than 0.5 % on the zirconia supports, showing that these catalysts were highly selective towards methanol. Silica had a detrimental support effect on the methanol formation rate, which primarily resulted from a drop in the total CO_2 conversion compared to bulk ZnO. This silica support has previously shown a similar negative effect on the turnover frequency for the methanol synthesis over Cu/SiO_2 compared to pure Cu (i.e. Raney Cu) [29]. Infrared spectroscopy of CO on Cu/SiO_2 showed a blueshift in the C-O frequency, hence the silica exerted an electron withdrawing effect upon Cu [30], which correlated to low activity of Cu/SiO_2. It is hypothesised that similar electronic interactions between SiO_2 and ZnO might cause the loss in activity when zinc oxide is supported on silica.

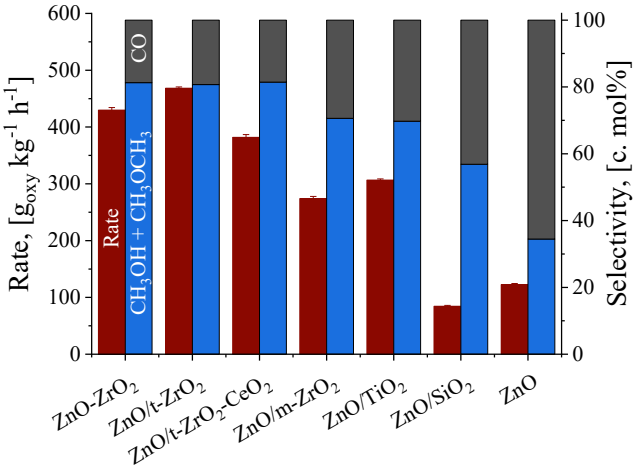

Fig. 1. The oxygenate (CH_3OH + CH_3OCH_3) formation rate for ZnO supported on different metal oxides (Zn mol% = 13) compared to the co-precipitated ZnO-ZrO_2 and pure ZnO. Conditions: 320 °C, 50 barg, 15 NL/h, catalyst loading of 300 mg, feed gas composition of CO_2/H_2/Ar 20/60/20.

As illustrated in Fig. 1, the mass-based activity and oxygenate selectivity for zinc oxide supported on titania and monoclinic zirconia showed similar results, all exerting a beneficial support effect. It was, therefore, necessary to clarify whether the beneficial supports indirectly affected an active ZnO phase on the surface or created particularly beneficial Zn^{2+} sites that are part of a solid solution with the support.

3.2. The importance of a ZnO surface phase for the catalytic activity

To elucidate the support effects, several samples with zinc oxide impregnated on tetragonal zirconia were prepared to understand the relation between zinc loading, activity and selectivity as illustrated in Fig. 2.

In Fig. 2 (a) the oxygenate formation rate was improved when increasing the Zn loading from 13 to 18 mol%, due to enhanced CO_2 conversion. Further increasing the Zn loading reduced the CO_2 conversion while maintaining the high selectivity towards methanol (Fig. 2 (b)). The major changes in catalytic properties with ZnO loading reflected changes in physical properties of the samples. The BET surface area, the amount of crystalline ZnO determined by Rietveld refinement of the XRD data, and the elemental bulk and surface composition from ICP-OES and XPS analysis are summarized in Table 1. The XRD patterns for the impregnated and co-precipitated samples are shown in Fig. 3.

Fig. 3 (a) shows that with increasing zinc loading by impregnation, the tetragonal (1 0 1) Bragg reflection, observed at $2\theta = 30.2°$, did not shift to higher angles, which is typically observed for ZnO in ZrO_2 solid solutions [9]. This shows that the tetragonal zirconia was unaffected and that no Zn was incorporated into the lattice. Furthermore, the high surface zinc fraction determined by XPS compared to the bulk zinc fraction suggests that zinc oxide was mainly deposited on the zirconia

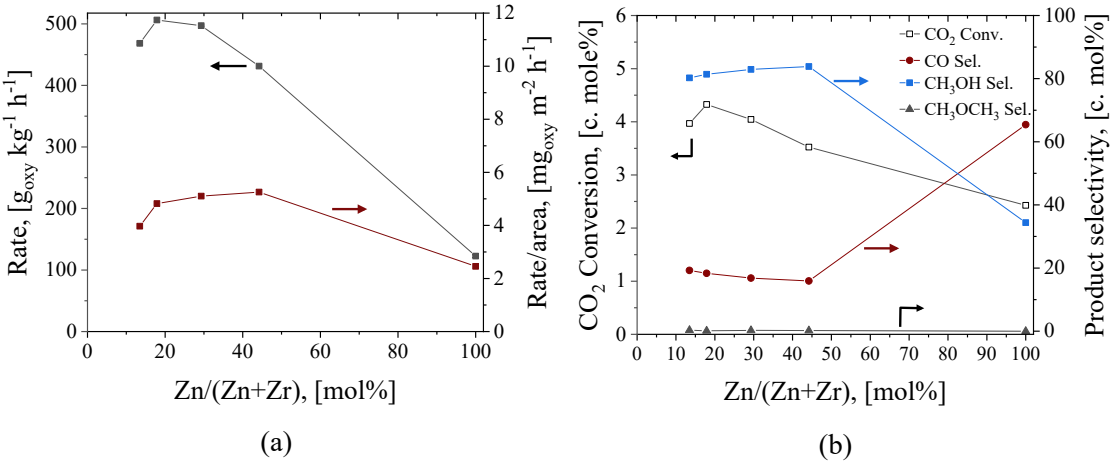

Fig. 2. (a) The oxygenate ($CH_3OH + CH_3OCH_3$) formation rate against mol% of Zn for ZnO supported on t-ZrO_2 based on catalyst mass (black) and surface area (red). (b) The CO_2 conversion (left axis), CH_3OH, CH_3OCH_3 and CO selectivity (right axis) against the mol% of Zn supported on tetragonal zirconia. Conditions: 320 °C, 50 barg, 15 NL/h, catalyst loading of 300 mg, feed gas composition of $CO_2/H_2/Ar$ 20/60/20.

Table 1
Specific surface area (BET), bulk Zn mol%, surface Zn mol%, the weight% of crystalline hexagonal ZnO, and the amount of surface oxygen vacancies relative to the total amount of oxygen. Numbers in parentheses represent analysis of spent samples.

Catalyst	BET	Bulk Zn/(M + Zn)[a]	Crystalline ZnO[b]	Surface Zn/(Zr + Zn)[c]	O_v/O_T [c]
Name	[m^2/g]	[mol%]	[wt%]	[mol%]	[%]
ZnO	49.9	100	100	100	29
(0.13)ZnO/t-ZrO_2	118	13.4	0 (0)	23	42
(0.18)ZnO/t-ZrO_2	105	17.9	0.7 (0.9)	30 (32)	43 (37)
(0.29)ZnO/t-ZrO_2	97.4	29.3	11 (7.9)	32	49
(0.44)ZnO/t-ZrO_2	82.1	44.2	21 (20)	38	39
ZnO/t-ZrO_2-CeO_2	77.3	13.4	2.2 (2.4)	–	–
ZnO/m-ZrO_2	44.8	13.5	5.4 (5.1)	–	–
ZnO/TiO_2	103	13.3	5.3 (6.5)	–	–
ZnO/SiO_2	165	13.0	1 (1.1)	–	–
ZnO-ZrO_2	40.3	10.7	0 (0)	33 (31)	45 (30)
ZnO-ZrO_2-100	145	12.0	0 (0)	22	37
t-ZrO_2	145	0	0	0	43

[a]Determined by ICP-OES, [b]determined by Rietveld refinement of XRD data, [c]determined by XPS where subscript V and T denotes the oxygen vacancies (defects) and total oxygen.

surface for the impregnated samples (Table 1). The fact that a comparatively high activity was achieved with the impregnated ZnO/t-ZrO_2 samples (Fig. 1 and Fig. 2) which on the basis of XPS/XRD did not show any sign of Zn incorporated as solid solution with the ZrO_2 support, suggests that the catalytic activity arised from a ZnO-type surface layer.

An increase from 13 to 18 mol% zinc enhanced the activity (Fig. 2 (a)) reflected in an increased CO_2 conversion at similarly high methanol selectivity (Fig. 2 (b)). At 18 mol% zinc, small amounts of crystalline ZnO were visible by XRD and the amount rose as the zinc loading increased (Fig. 3 (a)). Assuming an atom density like the bulk ZnO (0001) facet, ~19 mol% Zn would saturate the surface of the t-ZrO_2 support, with a specific surface area of 145 m^2/g, with a ZnO monolayer. Thus, it was consistent that this level marks the transition from a 2D ZnO surface phase to 3D ZnO nanoparticles. Scanning transmission electron microscopy with EDX of the impregnated sample with 13 mol% Zn (i.e. in the range of a 2D ZnO phase) showed well dispersed ZnO (Fig. S13). Fig. 4 (a) illustrates that the ZnO surface layer was in the form of surface domains with a diameter of ~ 5 nm. High-resolution transmission electron microscopy in Fig. 4 (b) showed a lattice spacing of 2.98 Å, similar to the lattice spacing of the (1 0 1) Bragg reflection of tetragonal zirconia (Fig. S14). No evidence of any crystalline structure of ZnO was found, which supports that the ZnO surface layer is an amorphous phase without an ordered 3D structure.

Fig. 2 (a) shows that the evolution of a 3D ZnO structure above 18 mol% Zn, did not improve the mass-based activity, but the activity per total catalyst surface area increased before dropping for bulk ZnO. The relative surface area occupied by crystalline ZnO nanoparticles increased as the zinc loading increased (Table 1), but the catalytic activity decreased, suggesting that the surface of the crystalline ZnO was less active. This shows that crystalline ZnO was of considerable activity on its own, but also that the ZnO surface layer dispersed on ZrO_2 was higher in activity, by a factor of at least 2 according to Fig. 2 (a). For the impregnated catalysts, XRD analyses of the spent samples showed a higher crystallinity, but no shift in the (1 0 1) Bragg reflection or changes in the tetragonal unit cell volume (Fig. 3 (a-c)), which remained close to the parent t-ZrO_2 support. This shows that the Zn in the samples remained as a ZnO surface phase during the reaction and did not migrate into the support, which was consistent with their activity being unaffected by the exposure to reaction conditions (Fig. 3 (c)).

The conclusion that activity arises from a ZnO surface layer and not from Zn^{2+} ions part of a solid solution with ZrO_2 is further substantiated by the behaviour of the co-precipitated ZnO-ZrO_2 samples. For the co-precipitated ZnO-ZrO_2 samples, the tetragonal zirconia unit cell volume was significantly lower than that for the impregnated samples (Fig. 3 (c)), suggesting that Zn^{2+} ions were present in the zirconia lattice, and this uptake of dopants that stabilized the tetragonal structure at temperatures below 1170 °C [13]. TEM analysis of the ZnO-ZrO_2 sample (Fig. S15) also supported that Zn was present as a mixture of both a highly dispersed Zn phase, consistent with isolated Zn^{2+} in a solid solution, and the ~ 5 nm ZnO surface domians seen for the impregnated

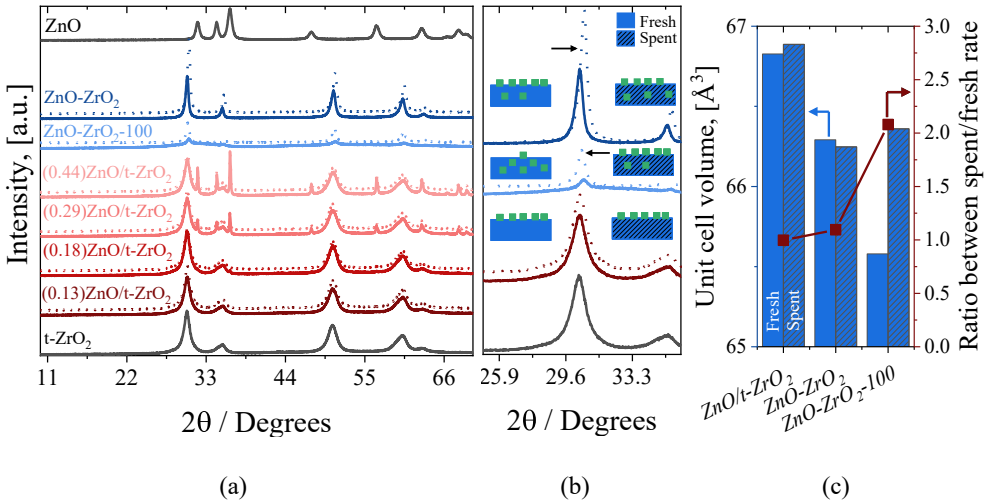

Fig. 3. (a) XRD patterns of ZnO supported on ZrO_2samples, bare t-ZrO_2 support and ZnO. (b) Zoom in on the (1 0 1) Bragg reflection of the fresh (solid line) and spent (dotted line) impregnated ZnO/t-ZrO2 (13 mol%), co-precipitated ZnO-ZrO2 at 70 °C and the co-precipitated ZnO-ZrO_2 at 100 °C. The arrow visualizes the (1 0 1) Bragg reflection movement from fresh to spent sample. The green boxes represent ZnO placed on the ZrO_2 surface or in the ZrO_2 structure, represented as blue box. (c) The unit cell volumes calculated from the lattice parameters obtained by Rietveld refinement and the spent to fresh reaction rate ratio at 300 °C and 50 bar, after exposure for 42 h to temperatures between 300 and 400 °C at 20 °C intervals.

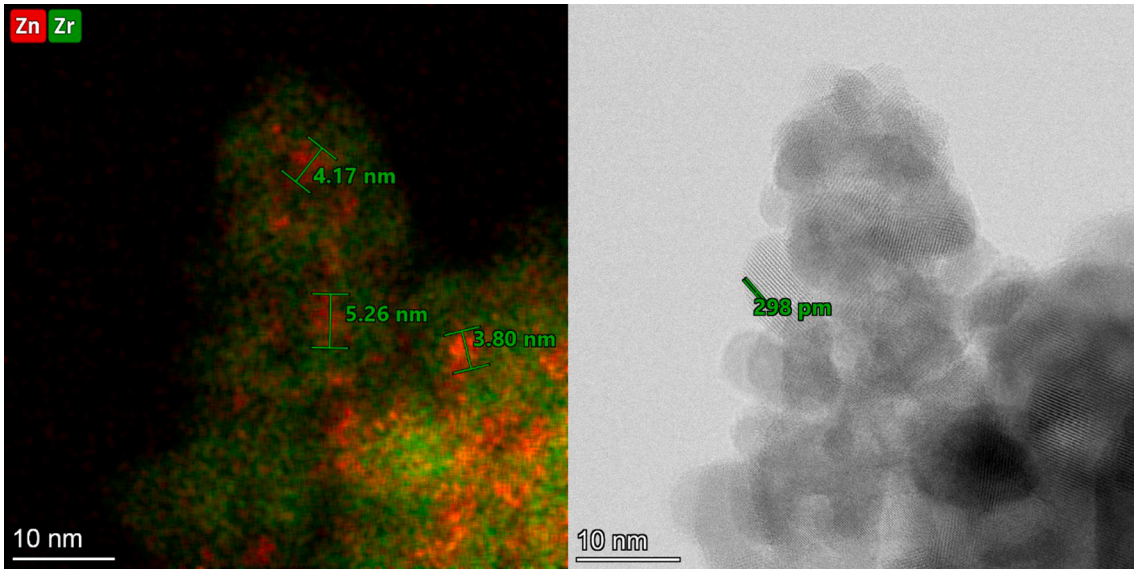

Fig. 4. (a) EDX element map of Zn and Zr of the image area in (b) high-resolution STEM image (bright field) of the (0.13)ZnO/t-ZrO_2 sample. The EDX quantification showed a mole fraction of Zn/(Zn + Zr) = 0.044 in this particular image area.

samples. The co-precipitated samples thus had some zinc arranged inside the zirconia structure, as has also been observed in several other studies [9,14–16]. The ZnO-ZrO_2-100 sample, co-precipitated at 100 ℃, had a particularly low unit cell volume (Fig. 3 (c)) and a relatively low surface ZnO content, close to the bulk composition (Table 1), which shows that this sample had a high degree of its Zn incorporated as solid solution. Two observations for the ZnO-ZrO_2-100 sample showed that Zn in the solid solution was not of particularly high catalytic activity. Firstly, Fig. 5 shows that ZnO-ZrO_2-100 had much lower initial activity than ZnO-ZrO_2, which had a higher surface enrichment of ZnO, although ZnO-ZrO_2-100 had a higher surface area. Secondly, the ZnO-ZrO_2-100 sample underwent a pronounced activation during the exposure to reaction conditions and after stabilization, the rate doubled compared to the initial level (Fig. 3 (c)). Analysis of the spent sample showed that this was mirrored by a downshift in the (1 0 1) Bragg reflection (Fig. 3 (b)) and a clear increase in unit cell volume (Fig. 3 (c)), which shows that the increased activity occurred when Zn segregated out of the solid solution and formed a ZnO surface layer, since crystalline ZnO was not observed.

Fig. 3 (b) shows an intensity increase in the XRD pattern for the t-ZrO_2 in ZnO-ZrO_2-100 during reaction, due to t-ZrO_2 becoming more crystalline and that the average crystallite size increased from about 100 to 186 Å according to Rietveld analysis, which would also result in a significant reduction of the specific surface area. Changes in the crystalline phase of the zirconia have previously resulted in an improved methanol synthesis performance [31,32]. However, the magnitude of these improvements is not comparable to the factor of > 2 in the oxygenate formation rate observed from the fresh to the spent ZnO-ZrO_2-100 in Fig. 3 (c). These findings are summarized in Fig. 5, showing that the two co-precipitated catalysts had similar total amount of ZnO according to ICP, but it is the catalyst with the highest amount of surface ZnO which is most active, despite its specific surface area being much lower. This shows that it is the surface ZnO and not Zn^{2+} ions in a solid

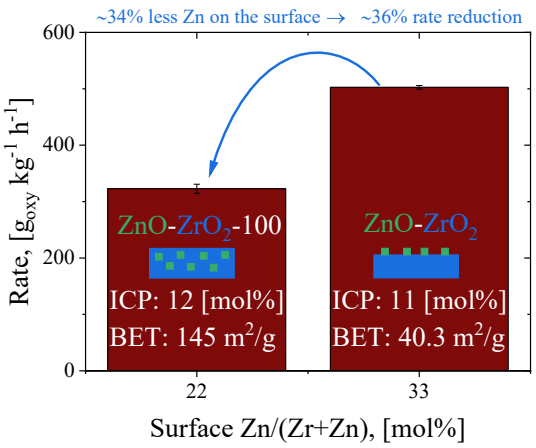

Fig. 5. The oxygenate (CH_3OH + CH_3OCH_3) formation rate against the mol% of ZnO supported on the ZrO_2 surface. Conditions: 320 °C, 50 barg, 32.1 NL/h, catalyst loading of 750 mg, feed gas composition of CO_2/CO/H_2/Ar 29/4/64/3.

solution, which is responsible for catalysing the methanol synthesis.

3.3. Local zinc oxide environment on the zirconia surface

Due to the amorphous nature of the ZnO surface domains on the ZrO_2 surface, XAS was conducted to characterize and quantify these species and evaluate their relation to the catalytic activity. The Zn K-edge X-ray absorption near edge structure (XANES) and the k^3-weighted Fourier-transformed extended X-ray absorption fine structure (FT-EXAFS) spectra of the as-prepared ZnO on ZrO_2 catalysts, Zn foil, and bulk ZnO are presented in Fig. 6(a) and (b), respectively. The XANES spectra (Fig. 6 (a)) shows the absorption edge at 9662 eV for the all ZnO/ZrO_2 samples, the same as bulk ZnO (9662 eV) rather than metallic Zn (9659 eV) [15,21]. The absence of a signal related to metallic Zn (Zn-Zn at approximately 2.2 Å) in the FT-EXAFS spectra (Fig. 6 (b)) confirmed that Zn^{2+} was the only oxidation state present in all the catalysts. At low Zn loadings ≤ 18 mol%, trends associated with ZnO were observed in the shape of the XANES spectra, but no signal related to the backscattering of the next nearest neighbour Zn-Zn was visible in the FT-EXAFS spectra. This indicated that the ~ 5 nm ZnO_x surface domains were a defective ZnO-phase with no repeating crystalline structure. As mentioned, the XPS evidence for surface enrichment of Zn (Table 1) revealed that these

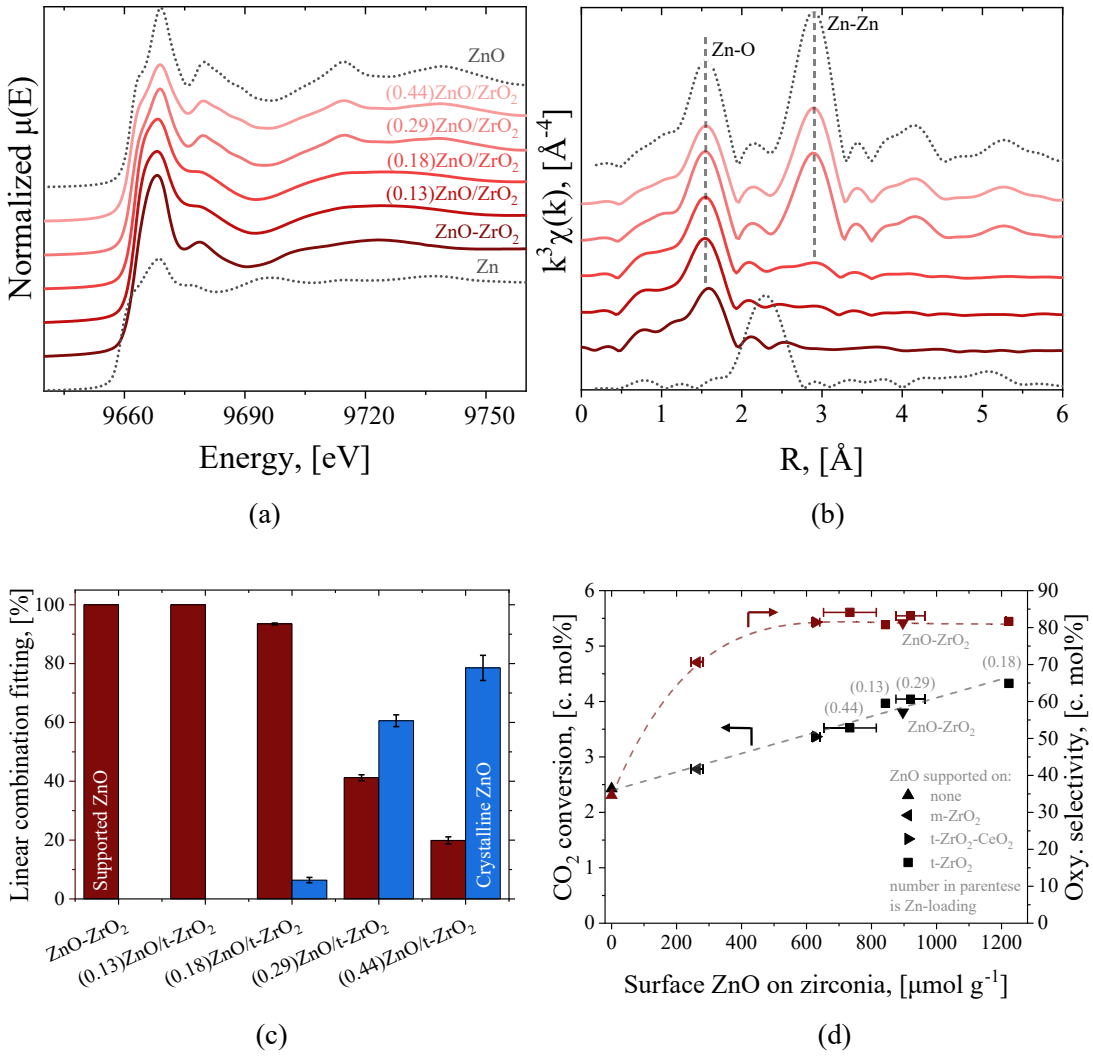

Fig. 6. (a) Zn K-edge XANES and (b) Fourier-transformed k^3-weighted EXAFS spectra of ZnO supported on zirconia catalysts with Zn foil and ZnO as references. (c) The fraction of surface ZnO determined by linear combination fitting (d) The CO_2 conversion and oxygenate (CH_3OH+CH_3OCH_3) selectivity against the calculated amount of surface ZnO species from Eq. (6). Reaction conditions: 320 °C, 50 barg, 15 NL/h, catalyst loading of 300 mg, feed gas composition of CO_2/H_2/Ar 20/60/20.

domains were present on the ZrO_2 surface. As the Zn loading increased > 18 mol% for the impregnated samples, the shape of the XANES spectra resembled that of bulk, hexagonal ZnO. This confirmed that an increasing fraction of the Zn created crystalline ZnO nanoparticles, as also detected with XRD. The co-precipitated ZnO-ZrO_2 sample showed similar trends as the Zn impregnated samples, but with more features in the XANES spectrum (Fig. 6 (a)). The combination of XRD (Fig. 3), XPS (Table 1) and TEM (Fig. S15) suggested that this sample had most of its Zn in the form of ZnO surface domains and a minority of its Zn in solid solution, where different atomic positions may not result in regular Zn-Zr distances. Therefore, no clear Zn-Zr backscattering at distance ≈ 3.5 Å was observed for this sample [33].

Fitting the EXAFS spectra (reported in Table S2) resulted in an interatomic distance of Zn-O ≈ 1.98 Å and of Zn-Zn ≈ 3.23 Å (only for Zn loadings > 18 mol%), similar to the distances observed for these two shells in pure hexagonal ZnO. Coordination numbers for the first Zn-O shell for the impregnated samples were close to 4, similar to bulk ZnO. A higher Zn-O coordination number would be expected if Zn^{2+} was incorporated into the zirconia lattice [34] or if the ZnO was hydrated. A decrease in the coordination number was seen with increasing Zn loading, which was caused by the strong correlation with the refined mean square deviation of interatomic distances (σ^2). The coordination number fit of the co-precipitated ZnO-ZrO_2 sample was lower. However, the standard deviation did not suggest any significant difference from the impregnated samples, suggesting that most of the Zn in this sample was in the presence of ZnO surface domains.

The fractions of Zn in the disordered ZnO domains and in crystalline 3D ZnO, respectively, were estimated by Eq. (5) using the coordination number of the Zn-Zn shell and by linear combination fitting of the XANES spectra between samples having only isolated domains (here (0.13)ZnO/t-ZrO_2) and bulk ZnO. Fig. 6 (c) shows the fraction of Zn in ZnO surface domains using the linear combination fitting method. Using the coordination number of the Zn-Zn shell, similar fractions of ZnO surface domains were determined. The result can be found in Table S2. With increasing Zn loading, more crystalline ZnO was formed, but a significant amount of the Zn was still present as ZnO surface domains. The amount of Zn present as ZnO surface domains was thus be determined from the results in Fig. 6 (c) and the total Zn loading of the sample using Eq. (6). On this basis, Fig. 6 (d) shows the CO_2 conversion and CO selectivity as function of the amount of surface ZnO. This illustrate that the surface ZnO was highly selective towards methanol formation and that the amount controlled the CO_2 conversion. Crystalline ZnO showed methanol formation activity, but, as illustrated in Fig. 6 (d), these sites had lower selectivity towards methanol. Assuming that the ZnO domains are 2D structures with all Zn-atoms exposed and that their site density was that of the crystalline ZnO(0001) facet, the results in Fig. 6 (d) show that the turnover frequency per Zn surface atom was 17 h^{-1} for ZnO domains and 4 h^{-1} for crystalline ZnO, respectively. Other Zn-containing catalysts have been prepared for other catalytic processes, where similar surface or isolated Zn^{2+} sites have been concluded to be the main active site [35–38], supporting the conclusion that supported ZnO provided the active sites for methanol synthesis.

As discussed in Section 3.3 the 18 mol% Zn sample contained an appropriate amount of Zn to cover the available ZrO_2 surface area, and above this value 3D ZnO nanoparticles of lower activity began to occupy part of the surface. Fig. 6 (d) illustrates that this sample was also the most active as it maximized the amount of ZnO surface sites. The results in Fig. 1 and Fig. 6 (d) thus reveal that activity of ZnO based methanol synthesis catalysts was maximized by choosing the optimal support, of which t-ZrO_2 was the best tested here, and loading with Zn to the maximal level at which a 2D ZnO surface layer could be maintained.

3.4. State of the ZnO surface domains and the nature of the support effect

Time resolved QEXAFS, coupled with modulation excitation spectroscopy (MES) to amplify spectral changes, was conducted to investigate the stability of the catalysts and to determine minute changes in the Zn oxidation state under methanol synthesis conditions. An initial dehydration step in O_2/He did not show any changes for the Zn oxidation state, but changes in the Zn K-edge XANES when switching to syngas could suggest partial Zn reduction (Fig. S10). To amplify this effect, MES experiments with periodic switching between a syngas mixture of CO_2/CO/H_2 (reducing gas) and an O_2/He mixture (oxidizing gas), with simultaneous measurements of spectra, were conducted. To conduct the MES analysis, the changes that occur when modulating the gas phase composition must be reversible. However, irreversible formation of crystalline ZnO was observed when switching between reducing and oxidizing atmospheres for the (0.18)ZnO/t-ZrO_2 and ZnO-ZrO_2 samples, which resulted in reduced methanol synthesis activity (Fig. S11). For the (0.13)ZnO/t-ZrO_2 sample, the first cycle resulted in an irreversible change in the XANES spectra, which stabilized from cycles 2 to 9, as illustrated in Fig. 7 (a), which shows the averaged time resolved spectra for 9 periods. The catalytic performance was stable throughout the 9 cycles, illustrated for the first 4 cycles in Fig. 7 (b), showing stable methanol synthesis activity (MS signal at $m/z = 31$, due to mass overlap O_2 also showed intensity at this mass). The averaged time resolved intensity at 9660 eV (for cycles 2 to 9) showed clear reversible changes in the intensity going from reducing to oxidizing conditions (Fig. S12). This allowed for the phase-domain analysis.

The phase-resolved spectra as obtained from averaged time resolved spectra shown in Fig. S12 (averaging cycles 2–9) are given in Fig. 7(c) at selected phase angles. The maximum intensity of phase resolved spectra was obtained at 150°, which was used for further comparison. The decreasing intensity at 9658–9660 eV, the edge position of metallic zinc, indicated reversible changes in the Zn oxidation state. In Fig. 7 (d), the phase-resolved spectrum at 150° phase angle scaled by a factor of 50 is compared to the difference spectrum between the as prepared sample and Zn foil. This shows a reversible partial reduction of Zn under reaction conditions, where approximately 1 out of 50 Zn atoms was reduced to a state closer to metallic Zn^0 than to Zn^{2+}. Thus, under reaction conditions, the ZnO surface species were partly reduced ZnO_x species with x approximately equal to 0.98. The partially reduced ZnO_x likely played an important role for the methanol synthesis activity. The thermodynamic reduction potentials of bulk ZnO to metallic Zn^0 from H_2 ($\Delta G = 78.5$ kJ/mol) and CO ($\Delta G = 63.8$ kJ/mol) show that this reaction is unlikely for bulk ZnO. The MES results thus indicated that the ZnO surface phase had an increased reducibility compared to crystalline bulk ZnO.

Fig. 8 shows the Zr 3d, Zn 2p and O 1 s XPS spectra for selected samples. In Fig. 8 (a), the spin–orbit doublet of the Zr 3d core level into Zr $3d_{5/2}$ and Zr $3d_{3/2}$ with binding energy around 182.5 and a splitting of ~ 2.5 eV, shows that the oxidation state was Zr^{4+} [39]. The impregnation of ZnO onto the zirconia support resulted in a shift for the Zr $3d_{5/2}$ to lower binding energies, indicating a charge enrichment of the ZrO_2 phase. In Fig. 8 (b), a spin–orbit doublet of Zn $2p_{3/2}$ and Zn $2p_{1/2}$ for pure ZnO were found at 1021 and 1044 eV, which shifted to higher binding energy when ZnO was supported on zirconia. This shift suggested that Zn^{2+} became more electron deficient. The position of the Zn LMM Auger peaks (Fig. S13) confirmed that Zn^{2+} was the only oxidation state present for all the samples. In Fig. 8 (c), the O 1 s peaks also shifted to lower binding energies compared to the bare t-ZrO_2 support, which supported that Zn^{2+} became more electron deficient. Lorentz peak fitting to the O 1 s peak for oxygen vacancies and lattice oxygen showed no relation between surface oxygen defects and the activity of the catalysts (Table 1). However, the binding energy values for all metals showed that there was an interaction between Zn and Zr. This interaction created a more electron deficient ZnO. Withdrawal of electrons from Zn-O bonds in the surface ZnO likely correlated with the increased partial reducibility of this phase to ZnO_x. This is further linked to the superior catalytic performance when ZnO was supported on ZrO_2, because it was easier to abstract oxygen from a more reducible ZnO_x surface and in that process oxophilic sites were created, that activated CO_2.

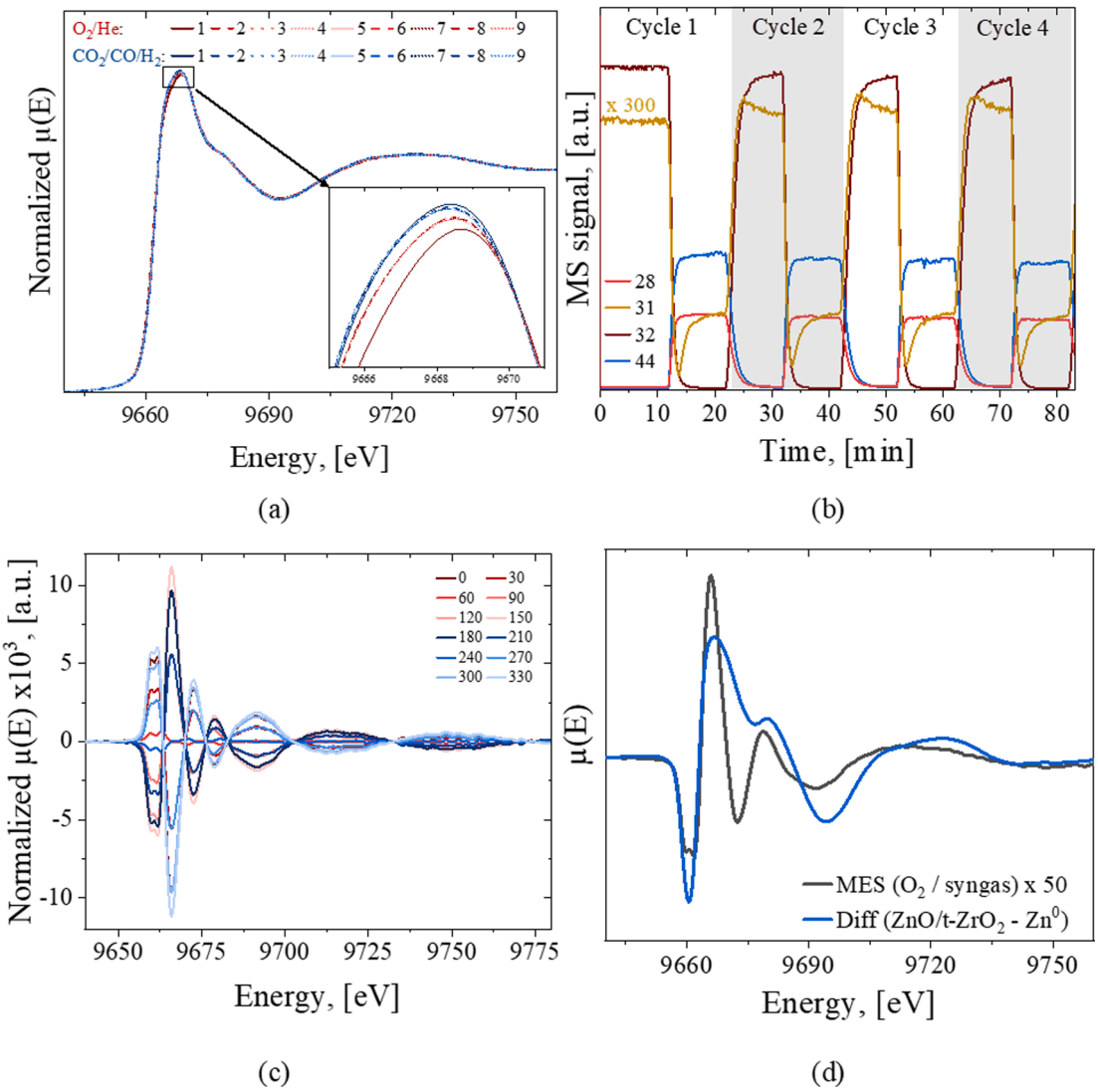

Fig. 7. (a) Zn K-edge XANES spectra of the (0.13)ZnO/t-ZrO_2 sample for cycles 1 to 9, where the gas was switched between O_2/He and syngas. (b) MS signal for the first 4 cycles showing the switch between gasses and the methanol formation. (c) The phase-resolved spectra obtained by Eq. (7) at different phase angles. (d) Comparison between the phase-resolved spectrum with the highest intensity (150°) with the difference spectrum of (0.13)ZnO/t-ZrO_2 minus Zn foil. Reaction conditions: 400 °C, 15 barg, 50 NmL/h, catalyst loading of ~ 2.5 mg (diluted 1:4 in inert α-Al_2O_3), feed gas composition of CO_2/CO/H_2/He 12/5/37/46.

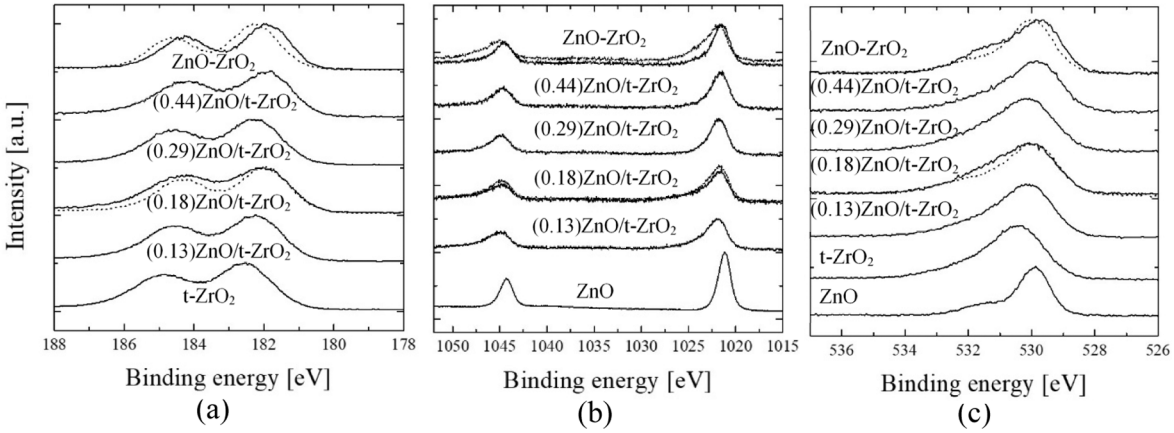

Fig. 8. XPS spectra of (a) Zr 3d, (b) Zn 2p and (c) O 1 s. Solid lines represent fresh catalysts samples, ZnO and bare t-ZrO_2 support, while dotted lines represent spent samples.

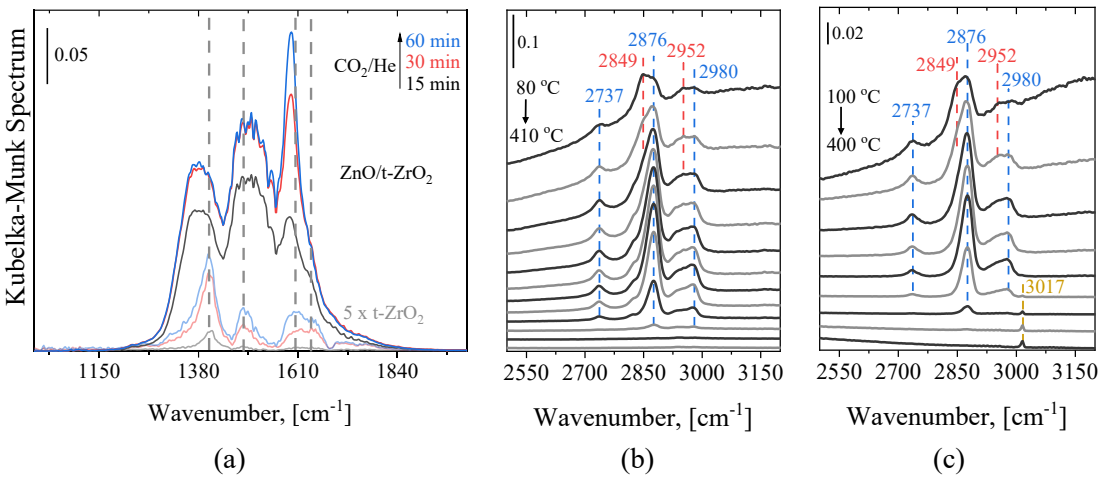

Fig. 9. In-situ DRIFTS measurements. (a) CO_2 adsorption on (0.13)ZnO/t-ZrO2 and bare t-ZrO_2 support at 20 bar and 320 °C. (b) TPD in He and (c) TPR in H_2 at 20 bar after steady-state methanol formation at 320 °C and 20 bar.

3.5. CO_2 hydrogenation reaction mechanism

In-situ DRIFTS was used to study the ZnO/t-ZrO_2 and t-ZrO_2 surface reaction intermediates for methanol formation from CO_2 and H_2. In Fig. 9 (a), the CO_2 adsorption on the t-ZrO_2 support lead to observation of bicarbonate and bridging carbonate species (HCO_3*, CO_3* with at 1404, 1484, 1604 and 1640 cm^{-1}) [37,40–42]. When ZnO was added to the support, strong signals attributed to bidentate formate (HCO_2* at 1360, 1382, 1595 and 2880 cm^{-1}) and zinc bonded carbonate (at 1508 cm^{-1}) adsorbates appeared [15,40,43]. The formation of formate species without H_2 present in the feed gas suggested that hydrogen was available at the zinc surface and that hydroxyl groups could play a role in the adsorption and activation of CO_2 [37]. After the CO_2 adsorption, the feed gas was changed to a H_2/He mixture and the intensity of the formate signal intensified and additional formate peaks at 2734, and 2978 cm^{-1} became visible. The carbonate signals (at 1404, 1484, 1508 and 1640 cm^{-1}) decreased, demonstrating hydrogenation of the carbonate species into formate [44]. With t-ZrO_2 alone, the formate signals were observed at lower wavenumbers and the carbonate species were still visible after 60 min (Fig. S18). Thus, having ZnO on the zirconia surface provided alternative formate and carbonate binding sites and improved the hydrogenation of the carbonate species into formate. This shows that the surface ZnO_x domains were able to bind and activate CO_2, while Zr-sites did not activate CO_2. Furthermore, no correlation between surface oxygen defects and activity was found by XPS analysis. In combination, the XPS and DRIFTS results contradicted that Zr should provide oxygen vacancies that operate in synergy with Zn for the formation of methanol as suggested elsewhere [33,45–47].

Fast removal of the carbonate species by hydrogenation into formate and further into methanol occurred when switching from CO_2 to H_2 at 320 °C. As the methanol formation subsided, the intensity of the formate peaks decreased, which suggested a pathway from HCOO to CH_3OH. However, formate signals were still visible at the catalyst surface at low methanol concentration (Fig. S17).

The (0.13)ZnO/t-ZrO_2 catalyst was subjected to steady-state methanol synthesis at 320 °C and 20 bar and then cooled to room temperature. Upon cooling, methoxy species (2849 and 2952 cm^{-1}) became visible at the catalyst surface [15,43]. Fig. 9 (b) and (c) show the results when this cooled sample was subjected to either temperature programmed desorption (TPD) in He or temperature programmed reaction (TPR) in H_2. The methoxy signals quickly disappeared when the reactor was heated in He or H_2, and were completely removed around 140 °C. This indicated that the pathway to methanol proceeds via methoxy, but that the hydrogenation of such species was so rapid that they were only visible at low temperatures. By further heating in He the carbonate species desorbed and were removed at around 220 °C. In H_2 atmosphere, the removal of carbonate species occurred at 180 °C (Fig. S19). The lower temperature for carbonate removal in the presence of H_2 suggested that carbonate was hydrogenated to formate instead of desorbing from the surface. Around 370 °C, the formate signals disappeared showing the bonding strength order of HCO_2*>CO_3*/HCO_3*>CH_3O*. As illustrated in Fig. S19, additional carbonate signals (at 1437 and 1573 cm^{-1}) became visible after formate desorption in He. These were concluded not to be relevant for the methanol synthesis activity as they are too strongly adsorbed on the surface, needing more than 410 °C to desorb. However, these signals were not observed in the H_2 atmosphere, suggesting that these carbonate species could be important for the methane formation.

These findings lead to the proposed reaction mechanism consisting of CO_2 adsorption as carbonate, hydrogenation into formate and further into methoxy and finally methanol. Formate was strongly adsorbed and accumulated on the catalyst surface. Hydrogenation of formate formed short lived adsorbed methoxy, which rapidly hydrogenated and desorbed as methanol. The loosely adsorbed methoxy and the fact that carbonate hydrogenates into formate in H_2 atmosphere before desorption, suggested that the hydrogenation of formate into methoxy was the rate-determining step, similar to that found for the Cu/ZnO/Al_2O_3 catalyst [48].

4. Conclusions

ZnO supported on zirconia materials were highly active and selective catalysts for high temperature methanol synthesis, making them good candidates for combinations with zeolites in a bifunctional process for direct conversion of CO_2 into hydrocarbon products. Impregnated samples showed similar selective performance towards methanol formation as the co-precipitated samples, without any integration of Zn into the zirconia lattice as detected by XRD. Hence, a solid solution of ZnO in ZrO_2 was not important for the catalytic activity or selectivity. Both preparation methods resulted in catalysts where ZnO was mainly present on the zirconia surface, as determined by XPS. Furthermore, only amorphous, surface ZnO was detected by XAS at low Zn loadings. Activity measurements of two co-precipitated samples with the same bulk Zn mol%, but with a significant difference in the surface Zn concentration, demonstrated the importance of ZnO located on the zirconia surface. TEM analysis showed well-dispersed ZnO as domains of ~ 5 nm size on the zirconia surface for the co-precipitated and impregnated samples, without ZnO adopting any crystalline structure. Modulation excitation spectroscopy coupled time resolved QEXAFS showed that these Zn sites were capable of reversible, partial reduction under

methanol synthesis conditions forming ZnO_x, where x was approximately 0.98. In-situ DRIFTS analysis of CO_2 adsorption under methanol synthesis conditions showed a shift in the formed carbonate and formate species on the ZnO containing zirconia, compared to the bare zirconia support. Together, these findings suggested that the active phase was the partly reduced surface ZnO_x, which adsorbed CO_2, hydrogenated it into formate and further into methanol.

CRediT authorship contribution statement

M.T. Nikolajsen: Conceptualization, Data curation, Writing – original draft, Visualization, Investigation, Formal analysis, Methodology. **J.-C. Grivel:** Writing – review & editing, Investigation, Data curation, Methodology. **A. Gaur:** Writing – review & editing, Methodology, Investigation, Formal analysis, Data curation. **L.P. Hansen:** Writing – review & editing, Investigation, Data curation, Methodology. **L. Baumgarten:** Writing – review & editing, Investigation, Data curation. **N.C. Schjødt:** Writing – review & editing, Supervision, Investigation, Conceptualization. **U.V. Mentzel:** Writing – review & editing, Supervision, Investigation, Conceptualization. **J.-D. Grunwaldt:** Writing – review & editing, Supervision, Investigation, Conceptualization. **J. Sehested:** Writing – review & editing, Supervision, Investigation, Conceptualization. **J.M. Christensen:** Writing – review & editing, Supervision, Methodology, Investigation, Formal analysis, Data curation, Conceptualization. **M. Høj:** Writing – review & editing, Supervision, Project administration, Methodology, Investigation, Funding acquisition, Formal analysis, Data curation, Conceptualization.

Declaration of competing interest

The authors declare that they have no known competing financial interests or personal relationships that could have appeared to influence the work reported in this paper.

Data availability

Data will be made available on request.

Acknowledgment

This work was funded by the Independent Research Fund Denmark (Grant no. 0136-00073B). We acknowledge the Paul Scherrer Institut, Villigen, Switzerland for provision of synchrotron radiation beamtime at beamline SuperXAS of the SLS (proposal no. 20220357). Funding for travels to SLS was provided by SPP2080 (DFG) and DanScatt. Special thanks are given to Eva S. Kold, Amalie B. Møller and Dr. Thomas Eldridge for their support overseeing experiments conducted at SLS and Simon Ingeman Hansen for his help making the graphical abstract.

Appendix A. Supplementary data

Supplementary data to this article can be found online at https://doi.org/10.1016/j.jcat.2024.115389.

References

[1] R. Geyer, J.R. Jambeck, K.L. Law, Production, use, and fate of all plastics ever made, Sci. Adv. 3 (2017) 25–29, https://doi.org/10.1126/sciadv.1700782.
[2] OECD, Global Plastics Outlook: Plastics use by region - projections, OECD Environ. Stat. (2022). https://doi.org/10.1787/913b14f3-en (accessed September 22, 2022).
[3] OECD, Global Plastics Outlook: Plastics use by polymer - projections, OECD Environ. Stat. (2022). https://doi.org/10.1787/b9bae4d1-en (accessed September 22, 2022).
[4] J.M. Garcia, M.L. Robertson, The future of plastics recycling, Science (80-.) 358 (2017) 870–872, https://doi.org/10.1126/science.aaq0324.
[5] X. Liu, M. Wang, H. Yin, J. Hu, K. Cheng, J. Kang, Q. Zhang, Y. Wang, Tandem catalysis for hydrogenation of CO and CO2 to lower olefins with bifunctional catalysts composed of spinel oxide and SAPO-34, ACS Catal. 10 (2020) 8303–8314, https://doi.org/10.1021/acscatal.0c01579.
[6] X. Liu, M. Wang, C. Zhou, W. Zhou, K. Cheng, J. Kang, Q. Zhang, W. Deng, Y. Wang, Selective transformation of carbon dioxide into lower olefins with a bifunctional catalyst composed of ZnGa2O4 and SAPO-34, Chem. Commun. 54 (2017) 140–143, https://doi.org/10.1039/c7cc08642c.
[7] M.B. Fichtl, D. Schlereth, N. Jacobsen, I. Kasatkin, J. Schumann, M. Behrens, R. Schlögl, O. Hinrichsen, Kinetics of deactivation on Cu/ZnO/Al2O3 methanol synthesis catalysts, Appl. Catal. A Gen. 502 (2015) 262–270, https://doi.org/10.1016/j.apcata.2015.06.014.
[8] D.L.S. Nieskens, J.D. Lunn, A. Malek, Understanding the enhanced lifetime of SAPO-34 in a direct syngas-to-hydrocarbons process, ACS Catal. 9 (2019) 691–700, https://doi.org/10.1021/acscatal.8b03465.
[9] J. Wang, G. Li, Z. Li, C. Tang, Z. Feng, H. An, H. Liu, T. Liu, C. Li, A highly selective and stable ZnO-ZrO2 solid solution catalyst for CO2 hydrogenation to methanol, Sci. Adv. 3 (2017) 1–11, https://doi.org/10.1126/sciadv.1701290.
[10] Y. Wang, L. Tan, M. Tan, P. Zhang, Y. Fang, Y. Yoneyama, G. Yang, N. Tsubaki, Rationally designing bifunctional catalysts as an efficient strategy to boost CO2 hydrogenation producing value-added aromatics, ACS Catal. 9 (2019) 895–901, https://doi.org/10.1021/acscatal.8b01344.
[11] H. Song, D. Laudenschleger, J.J. Carey, H. Ruland, M. Nolan, M. Muhler, Spinel-structured ZnCr2O4 with excess zn is the active ZnO/Cr2O3 catalyst for high-temperature methanol synthesis, ACS Catal. 7 (2017) 7610–7622, https://doi.org/10.1021/acscatal.7b01822.
[12] O. Martin, A.J. Martín, C. Mondelli, S. Mitchell, T.F. Segawa, R. Hauert, C. Drouilly, D. Curulla-Ferré, J. Pérez-Ramírez, Indium oxide as a superior catalyst for methanol synthesis by CO2 hydrogenation, Angew. Chemie - Int. Ed. 55 (2016) 6261–6265, https://doi.org/10.1002/anie.201600943.
[13] R.P. Ingel, D.L. Iii, Lattice parameters and density for Y2O3-stabilized ZrO2, J. Am. Ceram. Soc. 69 (1986) 325–332, https://doi.org/10.1111/j.1151-2916.1986.tb04741.x.
[14] Z. Han, C. Tang, F. Sha, S. Tang, J. Wang, C. Li, CO2 hydrogenation to methanol on ZnO-ZrO2 solid solution catalysts with ordered mesoporous structure, J. Catal. 396 (2021) 242–250, https://doi.org/10.1016/j.jcat.2021.02.024.
[15] S. Tada, N. Ochiai, H. Kinoshita, M. Yoshida, N. Shimada, T. Joutsuka, M. Nishijima, T. Honma, N. Yamauchi, Y. Kobayashi, K. Iyoki, Active sites on ZnxZr1– x O2–x solid solution catalysts for CO2 -to-methanol hydrogenation, ACS Catal. 12 (2022) 7748–7759, https://doi.org/10.1021/acscatal.2c01996.
[16] J. Ding, Z. Li, W. Xiong, Y. Zhang, A. Ye, W. Huang, Structural evolution and catalytic performance in CO2 hydrogenation reaction of ZnO-ZrO2 composite oxides, Appl. Surf. Sci. 587 (2022), https://doi.org/10.1016/j.apsusc.2022.152884.
[17] S. Pradhan, B.G. Mishra, Catalytic application of SO42-/fe-ZrO2 nanoparticles synthesized by a urea hydrolysis method for environmentally benign one pot synthesis of 1,8-dioxodecahydroacridines, RSC Adv. 5 (2015) 86179–86190, https://doi.org/10.1039/c5ra11136f.
[18] S. Vasanthavel, S. Kannan, Structural investigations on the tetragonal to cubic phase transformations in zirconia induced by progressive yttrium additions, J. Phys. Chem. Solids. 112 (2018) 100–105, https://doi.org/10.1016/j.jpcs.2017.09.010.
[19] S. Aghabeygi, M. Khademi-Shamami, ZnO/ZrO2 nanocomposite: sonosynthesis, characterization and its application for wastewater treatment, Ultrason. Sonochem. 41 (2018) 458–465, https://doi.org/10.1016/j.ultsonch.2017.09.020.
[20] C. Wang, G. Garbarino, L.F. Allard, F. Wilson, G. Busca, M. Flytzani-Stephanopoulos, Low-temperature dehydrogenation of ethanol on atomically dispersed gold supported on ZnZrOx, ACS Catal. 6 (2016) 210–218, https://doi.org/10.1021/acscatal.5b01593.
[21] S. Han, D. Zhao, T. Otroshchenko, H. Lund, U. Bentrup, V.A. Kondratenko, N. Rockstroh, S. Bartling, D.E. Doronkin, J.-D. Grunwaldt, U. Rodemerck, D. Linke, M. Gao, G. Jiang, E.V. Kondratenko, Elucidating the nature of active sites and fundamentals for their creation in zn-containing ZrO2-based catalysts for nonoxidative propane dehydrogenation, ACS Catal. 10 (2020) 8933–8949, https://doi.org/10.1021/acscatal.0c01580.
[22] K. Cheng, W. Zhou, J. Kang, S. He, S. Shi, Q. Zhang, Y. Pan, W. Wen, Y. Wang, Bifunctional catalysts for one-step conversion of syngas into aromatics with excellent selectivity and stability, Chem. 3 (2017) 334–347, https://doi.org/10.1016/j.chempr.2017.05.007.
[23] A.H. Clark, J. Imbao, R. Frahm, M. Nachtegaal, ProQEXAFS: a highly optimized parallelized rapid processing software for QEXAFS data, J. Synchrotron Radiat. 27 (2020) 551–557, https://doi.org/10.1107/S1600577519017053.
[24] B. Ravel, M. Newville, ATHENA, ARTEMIS, HEPHAESTUS: data analysis for X-ray absorption spectroscopy using IFEFFIT, J. Synchrotron Rad. 12 (2005) 537–541.
[25] A. Gaur, T.M. Hartmann Dabros, M. Høj, A. Boubnov, T. Prüssmann, J. Jelic, F. Studt, A.D. Jensen, J.-D. Grunwaldt, Probing the active sites of MoS 2 based hydrotreating catalysts using modulation excitation spectroscopy, ACS Catal. 9 (2019) 2568–2579, https://doi.org/10.1021/acscatal.8b04778.
[26] A. Gaur, M. Stehle, M. Serrer, M.Z. Stummann, C. La Fontaine, J.-D. Grunwaldt, M. Høj, Using transient XAS to detect minute levels of reversible S - O exchange at the active sites of MoS 2 – based hydrotreating catalysts : Effect of metal loading, promotion, temperature, and oxygenate reactant, ACS Catal. 12 (2022) 633–647, https://doi.org/10.1021/acscatal.1c04767.
[27] D. Baurecht, U.P. Fringeli, Quantitative modulated excitation fourier transform infrared spectroscopy, Rev. Sci. Instrum. 72 (2001) 3782–3792, https://doi.org/10.1063/1.1400152.
[28] A. Urakawa, T. Bürgi, A. Baiker, Sensitivity enhancement and dynamic behavior analysis by modulation excitation spectroscopy : principle and application in

heterogeneous catalysis, Chem. Eng. Sci. 63 (2009) 4902–4909, https://doi.org/10.1016/j.ces.2007.06.009.
[29] N.D. Nielsen, A.D. Jensen, J.M. Christensen, The roles of CO and CO2 in high pressure methanol synthesis over cu-based catalysts, J. Catal. 393 (2021) 324–334, https://doi.org/10.1016/j.jcat.2020.11.035.
[30] N.D. Nielsen, T.E.L. Smitshuysen, C.D. Damsgaard, A.D. Jensen, J.M. Christensen, Characterization of oxide-supported cu by infrared measurements on adsorbed CO, Surf. Sci. 703 (2021), https://doi.org/10.1016/j.susc.2020.121725.
[31] L. Lin, G. Wang, F. Zhao, CO2 hydrogenation to methanol on ZnO/ZrO2 catalysts : effects of zirconia phase, Chem. Sel. 6 (2021) 2119–2125.
[32] Z. Lui, Y. Ni, Z. Hu, Y. Fu, X. Fang, Q. Jiang, Z. Chen, W. Zhu, Z. Liu, Insights into effects of ZrO2 crystal phase on syngas-to-olefin conversion over ZnO/ZrO2 and SAPO-34 composite catalysts, chinese, J. Catal. 43 (2022) 877–884.
[33] D. Salusso, E. Borfecchia, S. Bordiga, Combining X-ray diffraction and X-ray absorption spectroscopy to unveil zn local environment in zn-doped ZrO2Catalysts, J. Phys. Chem. c. 125 (2021) 22249–22261, https://doi.org/10.1021/acs.jpcc.1c06202.
[34] G. Teufer, The crystal structure of tetragonal ZrO2., Aeta Cryst. (1962). 15 (1962) 1187.
[35] N.M. Schweitzer, B. Hu, U. Das, H. Kim, J. Greeley, L.A. Curtiss, P.C. Stair, J. T. Miller, A.S. Hock, Propylene hydrogenation and propane dehydrogenation by a single-site Zn2+ on silica catalyst, ACS Catal. 4 (2014) 1091–1098, https://doi.org/10.1021/cs401116p.
[36] J. Camacho-Bunquin, P. Aich, M. Ferrandon, A. "Bean" Getsoian, U. Das, F. Dogan, L.A. Curtiss, J.T. Miller, C.L. Marshall, A.S. Hock, P.C. Stair, Single-site zinc on silica catalysts for propylene hydrogenation and propane dehydrogenation: Synthesis and reactivity evaluation using an integrated atomic layer deposition-catalysis instrument, J. Catal. 345 (2017) 170–182. doi: 10.1016/j.jcat.2016.10.017.
[37] Y. Zro, E. Ko, M. Kogler, T. Bielz, B. Klo, S. Penner, In situ FT-IR spectroscopic study of CO2 and CO adsorption on Y2O3, ZrO2 and yttria-stabilized ZrO2, J. Phys. Chem. c. 117 (2013) 17666–17673.
[38] I. Pinilla-Herrero, E. Borfecchia, J. Holzinger, U.V. Mentzel, F. Joensen, K. A. Lomachenko, S. Bordiga, C. Lamberti, G. Berlier, U. Olsbye, S. Svelle, J. Skibsted, P. Beato, High Zn/Al ratios enhance dehydrogenation vs hydrogen transfer reactions of zn-ZSM-5 catalytic systems in methanol conversion to aromatics, J. Catal. 362 (2018) 146–163, https://doi.org/10.1016/j.jcat.2018.03.032.
[39] S. Tsunekawa, K. Asami, S. Ito, M. Yashima, T. Sugimoto, XPS study of the phase transition in pure zirconium oxide nanocrystallites, 252 (2005) 1651–1656. doi: 10.1016/j.apsusc.2005.03.183.
[40] S.E. Collins, M.A. Baltanás, A.L. Bonivardi, An infrared study of the intermediates of methanol synthesis from carbon dioxide over Pd/β -Ga2O3, J. Catal. 226 (2004) 410–421, https://doi.org/10.1016/j.jcat.2004.06.012.
[41] K. Pokrovski, K.T. Jung, A.T. Bell, Investigation of CO and CO 2 adsorption on tetragonal and monoclinic zirconia, Langmuir. 17 (2001) 4297–4303.
[42] S.M. Fehr, K. Nguyen, I. Krossing, Realistic operando-DRIFTS studies on Cu/ZnO catalysts for CO2 hydrogenation to methanol – direct observation of mono-ionized defect sites and implications for reaction intermediates, ChemCatChem. 14 (2022), https://doi.org/10.1002/cctc.202101500.
[43] Y. Wang, S. Kattel, W. Gao, K. Li, P. Liu, G.J. Chen, H. Wang, Exploring the ternary interactions in Cu–ZnO–ZrO2 catalysts for efficient CO2 hydrogenation to methanol, Nat. Commun. 10 (2019) 1–8, https://doi.org/10.1038/s41467-020-16342-1.
[44] L.F. Bobadilla, J.L. Santos, S. Ivanova, J.A. Odriozola, A. Urakawa, Unravelling the role of oxygen vacancies in the mechanism of the reverse water-gas shift reaction by operando DRIFTS and ultraviolet-visible spectroscopy, ACS Catal. 8 (2018) 7455–7467, https://doi.org/10.1021/acscatal.8b02121.
[45] P. Ticali, D. Salusso, R. Ahmad, C. Ahoba-Sam, A. Ramirez, G. Shterk, K. A. Lomachenko, E. Borfecchia, S. Morandi, L. Cavallo, J. Gascon, S. Bordiga, U. Olsbye, CO2 hydrogenation to methanol and hydrocarbons over bifunctional zn-doped ZrO2 /zeolite catalysts, Catal. Sci. Technol. 11 (2021) 1249–1268, https://doi.org/10.1039/d0cy01550d.
[46] C. Zhou, J. Shi, W. Zhou, K. Cheng, Q. Zhang, J. Kang, Y. Wang, Highly active ZnO-ZrO2 aerogels integrated with H-ZSM-5 for aromatics synthesis from carbon dioxide, ACS Catal. 10 (2020) 302–310, https://doi.org/10.1021/acscatal.9b04309.
[47] Y. Yang, G. Wang, M. Gong, F. Zhao, Effect of preparation methods of ZnO/ZrO2 catalysts for methanol synthesis from CO2 hydrogenation, React. Kinet. Mech. Catal. 135 (2022) 2993–3005, https://doi.org/10.1007/s11144-022-02298-4.
[48] M. Bowker, R.A. Hadden, H. Houghton, J.N.K. Hyland, K.C. Waugh, The mechanism of methanol synthesis on copper/zinc oxide/alumina catalysts, J. Catal. 109 (1988) 263–273, https://doi.org/10.1016/0021-9517(88)90209-6.